*molecules*

MDPI

*Article*

# Optimizing Metal Sites in Hierarchical USY for Selective Hydrocracking of Naphthalene to BTX

**Kunyi Zheng [1], Mingjia Liu [2], Haidong Li [1,2,*], Xiu Chen [1,2,*] and Xilong Wang [2,*]**

[1] School of Chemistry and Chemical Engineering, Linyi University, Linyi 276000, China; zhengkunyi2026@163.com
[2] State Key Laboratory of Heavy Oil Processing, China University of Petroleum, Beijing 102249, China; 13691005988@163.com
* Correspondence: lihaidong@lyu.edu.cn (H.L.); chenxiu@lyu.edu.cn (X.C.); wxl@cup.edu.cn (X.W.)

**Abstract**

Metal components (CoMo, NiMo, NiW) supported on hierarchical porous USY zeolite (HPY) were systematically optimized for selective naphthalene hydrocracking to BTX (benzene, toluene, xylene). The hierarchical porosity enhanced mass transport and accessibility to active metal sites, improving reaction selectivity and efficiency. Supported metal sulfides served as hydrogenation sites, crucial for aromatic ring activation and coke suppression. By optimizing the synergy between hydrogenation and cracking functions, the optimized $Ni_1W$/HPY catalyst achieved complete naphthalene conversion with a BTX yield of 92.5%. The spatial distribution of $WO_3$ crystallites facilitated functional separation, promoting selective conversion. These findings underscore the importance of metal–acid balance and pore architecture in designing efficient hydrocracking catalysts.

**Keywords:** hierarchical porous USY zeolite; bimetallic catalysts; naphthalene; selective hydrocracking; BTX

check for updates

Academic Editor: Boggavarapu Kiran

Received: 9 September 2025
Revised: 24 September 2025
Accepted: 30 September 2025
Published: 9 October 2025

**Citation:** Zheng, K.; Liu, M.; Li, H.; Chen, X.; Wang, X. Optimizing Metal Sites in Hierarchical USY for Selective Hydrocracking of Naphthalene to BTX. *Molecules* **2025**, *30*, 4023. https://doi.org/10.3390/molecules30194023

**Copyright:** © 2025 by the authors. Licensee MDPI, Basel, Switzerland. This article is an open access article distributed under the terms and conditions of the Creative Commons Attribution (CC BY) license (https://creativecommons.org/licenses/by/4.0/).

## 1. Introduction

The strategic upgrading of light cycle oil (LCO)—a low-value refinery stream rich in polycyclic aromatic hydrocarbons (PAHs) like naphthalene—into high-purity benzene, toluene, and xylene (BTX) addresses dual industrial priorities: mitigating environmental impacts from transportation fuels and meeting growing demand for petrochemical feedstocks [1–4]. This conversion represents a crucial pathway for enhancing the value of refinery streams while supporting the transition toward more sustainable chemical production. Selective hydrocracking of PAHs to BTX relies critically on bifunctional catalysts that synergize metal-catalyzed hydrogenation with acid-driven cracking [5–10]. The intricate balance between these two functions determines both catalytic activity and product distribution, making the design of such catalysts particularly challenging.

Hierarchical pore engineering in USY zeolites has emerged as a powerful strategy to enhance reactant diffusion and accessibility to active sites [11–13]. By introducing mesopores while preserving the intrinsic microporous structure, these modified zeolites overcome diffusion limitations that often plague conventional microporous catalysts when processing bulky molecules like PAHs. However, while pore architecture optimization has received significant attention, the strategic design of metal components (e.g., CoMo, NiMo, NiW) remains equally critical yet less explored. The choice of metal component fundamentally dictates catalytic efficiency and product distribution, as it influences hydrogenation activity, sulfidation degree, and metal–acid balance [14–22].

Recent studies have highlighted the importance of optimizing metal dispersion and acidity to minimize over-cracking and coke formation [23–28]. Shin et al. discovered that when loading metals with varying tetralin hydrogenation (HYD) activities on H-Beta, hydrocracking (HYC) catalysts containing moderate-HYD-activity metals (CoMo-S, NiMo-S) exhibited higher BTX through-yield than those with high-HYD-activity metals (Ni, NiSn, NiW-S) or monofunctional H-Beta catalysts [10]. Peng et al. [29] evaluated three bifunctional catalysts for LCO upgrading: Ni-W/HY-$Al_2O_3$, Ni-W/Hβ-$Al_2O_3$, and Ni-Mo/HY-$Al_2O_3$. The Ni-Mo/HY-$Al_2O_3$ system showed the highest hydrocracking ability attributed to its balanced acidity and uniform metal dispersion. These discrepancies highlight the need to correlate metal speciation (dispersion, sulfidation state) with acidity profiles in hierarchical frameworks. The spatial distribution of metal sites relative to acid centers appears particularly important for controlling reaction pathways. Despite these advances, the relationship between metal speciation, pore architecture, and catalytic performance in hierarchical USY supports remains insufficiently understood. Many studies focus either on metal function or acid function separately, without considering their spatial relationship within hierarchical pore systems.

This work aims to systematically address this knowledge gap by optimizing metal sites (CoMo, NiMo, NiW) on hierarchical porous USY zeolite (HPY) for selective naphthalene hydrocracking. We specifically investigate how metal type and loading influence the spatial distribution of active phases and how this distribution affects the critical metal–acid balance required for high BTX selectivity. Through a suite of characterization techniques (XRD, $N_2$ physisorption, TEM, XPS, $H_2$-TPR, $NH_3$-TPD, Py-FTIR) and catalytic evaluation, we elucidate the structure–activity relationships and identify the optimal metal composition for maximizing BTX yield.

## 2. Results and Discussion

### *2.1. Characterization of Catalysts*

#### 2.1.1. Structure Properties and Pore Structure

XRD patterns (Figure 1a) confirm the successful synthesis of the core–shell structures. Characterization of the synthesized catalysts provided deep insights into their structural and chemical properties, directly correlating with their performance in naphthalene hydrocracking. XRD analysis revealed distinct metal dispersion patterns. $Ni_2Mo$/HPY and $Co_2Mo$/HPY catalysts exhibited only the characteristic peaks of the USY structure, indicating highly dispersed Mo species. In contrast, $Ni_xW$/HPY catalysts displayed peaks at $2\theta = 23.1^\circ$ corresponding to crystalline $WO_3$, signifying W agglomeration [30]. Crucially, the intensity of the $WO_3$ peak was highest for $Ni_1W$/HPY and progressively decreased with increasing Ni loading ($Ni_2W$ to $Ni_5W$), suggesting that Ni promotes W dispersion on the HPY support at higher loadings.

Nitrogen physisorption further elucidated pore structure evolution (Figure 1b). While all catalysts exhibited type IV isotherms with H4 hysteresis loops (indicating particle-aggregation mesopores), pore size distributions revealed critical distinctions (Figure 1c). $Ni_2Mo$/HPY and $Co_2Mo$/HPY displayed broad mesopore distributions centered at ~7 nm, with moderate $S_{BET}$ (258–277 $m^2/g$), low $S_{mi}{}^c$ (170–194 $m^2/g$), low $V_{mi}{}^c$ (0.07–0.08 $cm^3/g$), and higher $V_{mes}$ (0.17–0.20 $cm^3/g$), confirming that their metal loading enhanced mesoporosity at the expense of microporosity [16].

In stark contrast, the $Ni_xW$/HPY series exhibited significantly higher $S_{BET}$ (536–548 $m^2/g$), $S_{mi}{}^c$ (427–439 $m^2/g$), and $V_{mi}{}^c$ (0.20–0.21 $cm^3/g$), alongside lower $V_{mes}$ (0.11–0.12 $cm^3/g$). Critically, these catalysts maintained >90% micropore retention. This superior microporosity preservation stems from the unique interaction between larger $WO_3$ crystallites inherent to NiW loading and the hierarchical pore architecture of the

USY support. Specifically, the larger $WO_3$ particles preferentially occupy mesopores and external surfaces, thereby minimizing blockage of the crucial micropore network essential for acid-catalyzed cracking. This selective deposition exposes more active sites accessible to nitrogen adsorption, increasing both measured microporous and mesoporous surface areas.

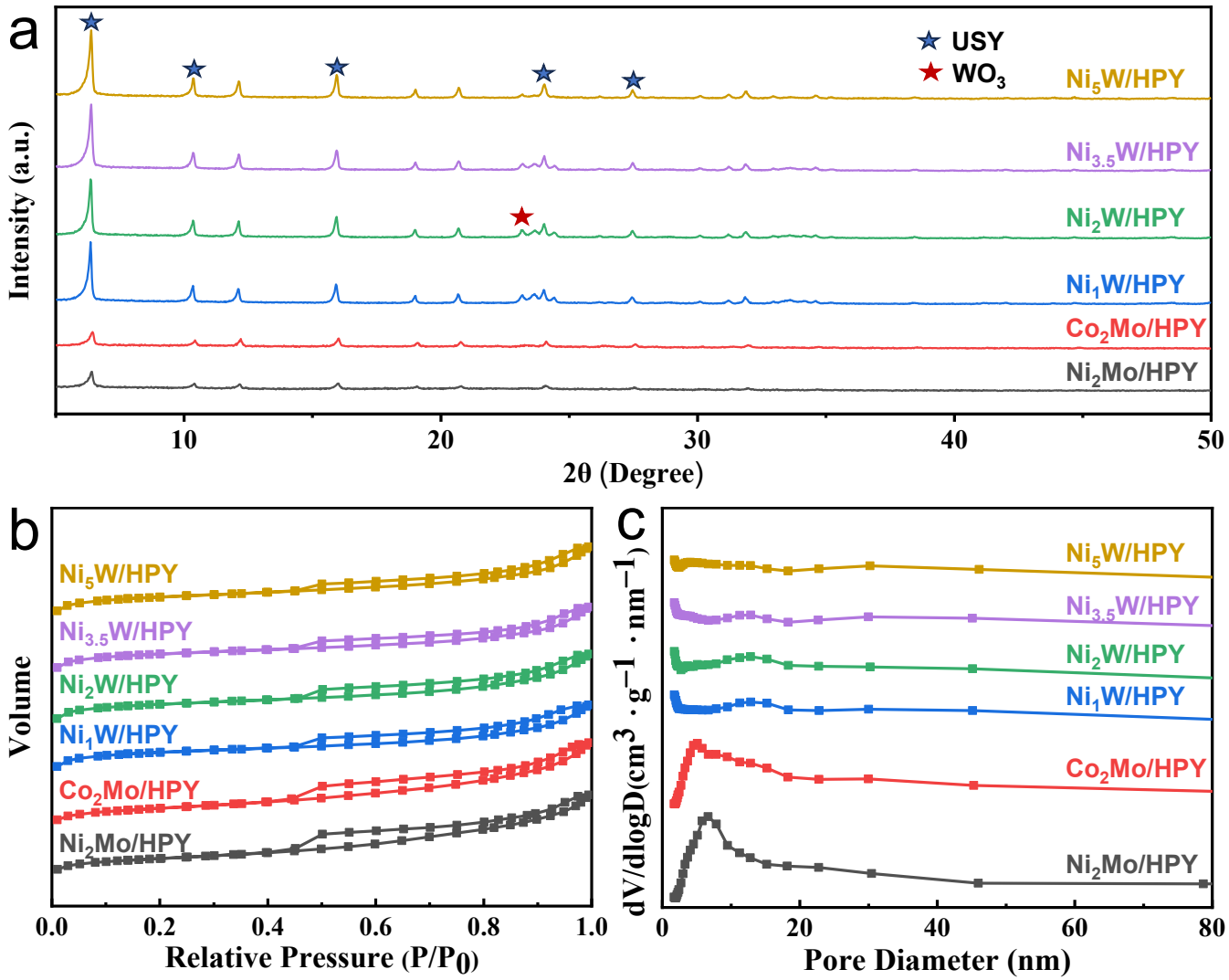



**Figure 1.** (**a**) Wide-angle XRD patterns, (**b**) $N_2$ physisorption isotherms, (**c**) pore width distribution of supports.

The preserved microporosity and strategic localization of metal species create a spatial segregation of functions: NiW active metals predominantly load onto the mesopores and external surfaces (regions with inherently lower acid site density), while the intact micropores house the strong Brønsted acidic cracking centers. This architectural optimization is essential for enforcing the desired sequential reaction pathway—initial hydrogenation of aromatic rings like naphthalene on the metal sites located in more open mesopores [31], followed by selective cracking of the hydrogenated intermediates (e.g., tetralin, decalin) within the sterically constrained micropores [32]. This bifunctional synergy, facilitated by the hierarchical USY structure interacting effectively with large W crystallites, enhances target product selectivity (Table 1).

**Table 1.** Pore Structure Parameters of $A_xB$/HPY Series Catalysts.

| Samples/HPY | Pore Size (nm) | $V_{total}$ ($cm^3/g$) | $V_{mic}$ ($cm^3/g$) | $V_{mes}$ ($cm^3/g$) | $S_{BET}$ ($m^2/g$) | $S_{mic}$ ($m^2/g$) | $S_{ext}$ ($m^2/g$) |
|---|---|---|---|---|---|---|---|
| HPY | 7.5 | 0.45 | 0.26 | 0.19 | 709 | 554 | 155 |
| $Ni_2Mo$ | 5.8 | 0.27 | 0.07 | 0.20 | 258 | 170 | 88 |
| $Co_2Mo$ | 6.5 | 0.25 | 0.08 | 0.17 | 277 | 194 | 83 |
| $Ni_1W$ | 7.0 | 0.32 | 0.20 | 0.12 | 536 | 427 | 109 |
| $Ni_2W$ | 7.2 | 0.33 | 0.21 | 0.12 | 548 | 437 | 111 |
| $Ni_3W$ | 7.3 | 0.31 | 0.20 | 0.11 | 540 | 434 | 106 |
| $Ni_5W$ | 7.4 | 0.32 | 0.20 | 0.12 | 539 | 433 | 106 |

#### 2.1.2. Microstructure and Morphology

TEM images confirmed the preservation of the intrinsic zeolite pore structure and morphology (slit-shaped pores, secondary pores) across all catalysts. No large metal agglomerates were readily observable, consistent with XRD indicating dispersion for NiMo/CoMo and suggesting that despite detectable $WO_3$ XRD peaks, W is partially dispersed, with agglomerates likely being small or electron-transparent (Figure 2).

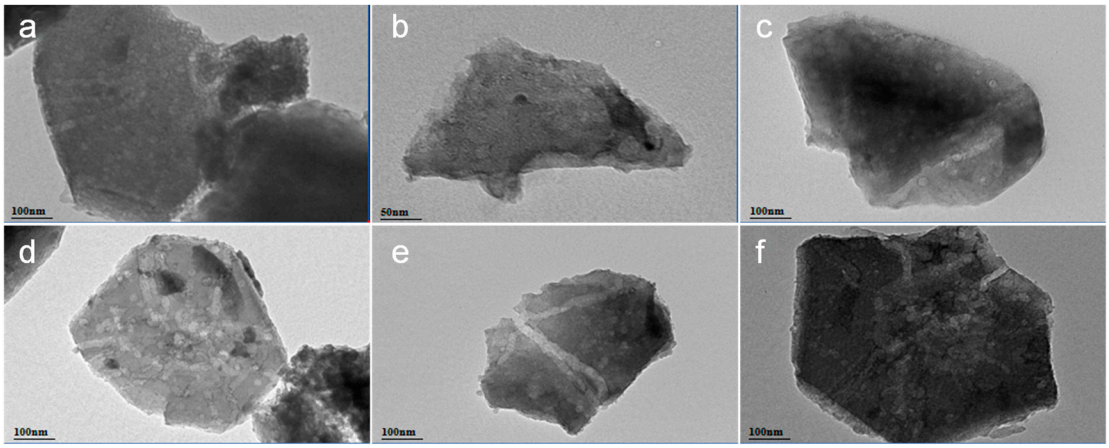



**Figure 2.** TEM image of $A_xB$/HPY series catalysts: (**a**) $Ni_2Mo$/HPY (**b**) $Co_2Mo$/HPY; (**c**) $Ni_1W$/HPY; (**d**) $Ni_2W$/HPY; (**e**) $Ni_{3.5}W$/HPY; (**f**) $Ni_5W$/HPY.

#### 2.1.3. Surface Acidity Properties of $A_xB$/HPY Catalysts

The acid properties of the Ni-loaded catalysts were characterized by $NH_3$-TPD (Figure 3a) and pyridine-adsorbed FTIR (Py-IR, Figure 3b), with quantitative acid type distribution and strength summarized in Table 2. Total acidity and medium/strong acidity were determined by Py-FTIR at 200 °C and 350 °C, respectively, while Py-IR analysis identified Lewis acid sites (L) via peaks at 1450 $cm^{-1}$ and 1610 $cm^{-1}$, Brønsted acid sites (B) at 1540 $cm^{-1}$, and overlapping Brønsted–Lewis sites (B + L) at 1490 $cm^{-1}$ [33–35]. The $Ni_2Mo$/HPY series exhibited the highest total acidity and strong acid density, followed by $Co_2Mo$/HPY, while the $Ni_xW$/HPY catalysts with varying Ni/W ratios consistently showed the lowest acid concentrations. Critically, excessive strong acidity (particularly Brønsted type) promotes undesired overcracking through β-scission and hydrogen transfer reactions, generating light hydrocarbons ($C_1$–$C_4$) at the expense of BTX yield due to accelerated coking and reduced aromatic selectivity.

#### 2.1.4. Metal–Support Interaction of $A_xB$/HPY Catalysts

$H_2$-TPR provided insights into reducibility and metal–support interactions (Figure 4). $Ni_2Mo$/HPY and $Co_2Mo$/HPY showed two main reduction peaks: a low-temperature peak (~420–520 °C) assigned to the reduction of octahedral $Mo^{6+}$ species to $Mo^{4+}$, and a high-temperature peak (~700–750 °C) for the further reduction of $Mo^{4+}$ to $Mo^0$ [36–38]. The

Co-promoted catalyst exhibited a more intense low-temperature peak shifted slightly higher, indicating enhanced Mo dispersion/sulfidation and a stronger interaction with the support, consistent with the XPS findings. For $Ni_xW/HPY$, $Ni_1W/HPY$ and $Ni_2W/HPY$ displayed only a high-temperature reduction peak (~750 °C) corresponding to $WO_3$ reduction, with no distinct reduction peak for NiO (~400 °C), confirming excellent Ni dispersion at these low loadings [39,40]. Catalysts with Ni loading ≥ 3.5 wt% ($Ni_{3.5}W/HPY$, $Ni_5W/HPY$) exhibited a clear NiO reduction peak around 400 °C, signifying Ni agglomeration. Furthermore, the $WO_3$ reduction peak shifted to lower temperatures with increasing Ni loading (from ~750 °C for $Ni_1W$ to lower temperatures for $Ni_5W$), signifying a weakening of the W–support interaction induced by Ni addition.

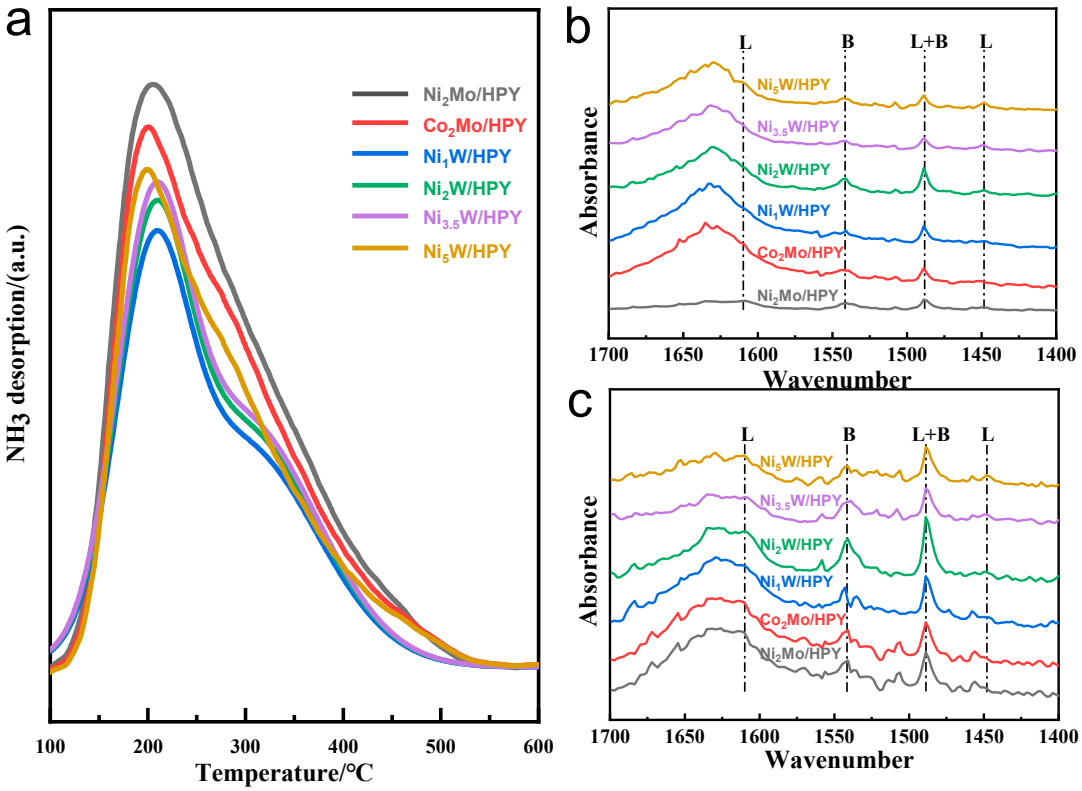



**Figure 3.** (**a**) NH3-TPD spectra of catalysts, (**b**) Py-IR spectra after desorbing at 200 °C, (**c**) Py-IR spectra after desorbing at 350 °C.

**Table 2.** Acid Properties of $A_xB/HPY$ Series Catalysts.

| Samples /HPY | Total Acid μmol/g | Weak Acid, μmol/g | | | Strong Acid, μmol/g | | |
|---|---|---|---|---|---|---|---|
| | | L | B | L + B | L | B | L + B |
| $Ni_2Mo$ | 619.2 | 72.0 | 158.1 | 230.1 | 165.7 | 223.4 | 389.1 |
| $Co_2Mo$ | 557.2 | 113.9 | 93.2 | 207.1 | 60.5 | 289.6 | 350.1 |
| $Ni_1W$ | 431.0 | 59.0 | 111.3 | 170.3 | 64.2 | 196.5 | 260.7 |
| $Ni_2W$ | 461.9 | 61.5 | 120.3 | 181.8 | 38.0 | 242.2 | 280.2 |
| $Ni_{3.5}W$ | 480.6 | 125.2 | 63.5 | 188.7 | 56.1 | 235.8 | 291.9 |
| $Ni_5W$ | 495.3 | 114.9 | 80.7 | 195.6 | 65.9 | 233.8 | 299.7 |

2.1.5. Chemical State Analysis of Active Phase

XPS analysis of sulfided catalysts focused on the chemical state of the active metals (Figure 5). Mo(W) XPS peak data of molybdenum (tungsten) species in sulfided AxB/HPY series catalysts summarized in Table 3. $Co_2Mo/HPY$ exhibited the highest sulfided $Mo^{4+}$

content (72.4%), significantly exceeding that of $Ni_2Mo/HPY$ (48.8%), indicating that Co promotes Mo sulfidation on the HPY support. XPS analysis of sulfided $Ni_xW/HPY$ catalysts revealed tungsten's complex speciation, where W 4f spectra deconvoluted into three distinct states: sulfided $W^{4+}$ ($WS_2$-like phase; W 4f5/2: 35.9 eV and W 4f3/2: 37.8 eV), partially sulfided $W^{5+}$ (oxo-sulfide intermediate; W 4f5/2: 36.5 eV and W 4f3/2: 38.3 eV), and oxidized $W^{6+}$ ($WO_3$-like; W 4f5/2: 38.7 eV and W 4f3/2: 39.0 eV) [41–43]. Critically, Ni loading exerted a non-monotonic influence: Low Ni loading ($Ni_1W/HPY$) maximized $W^{4+}$ content (70.25%) by weakening strong metal–support interactions (MSIs) through Ni-O-W bond formation, which enhanced reducibility.

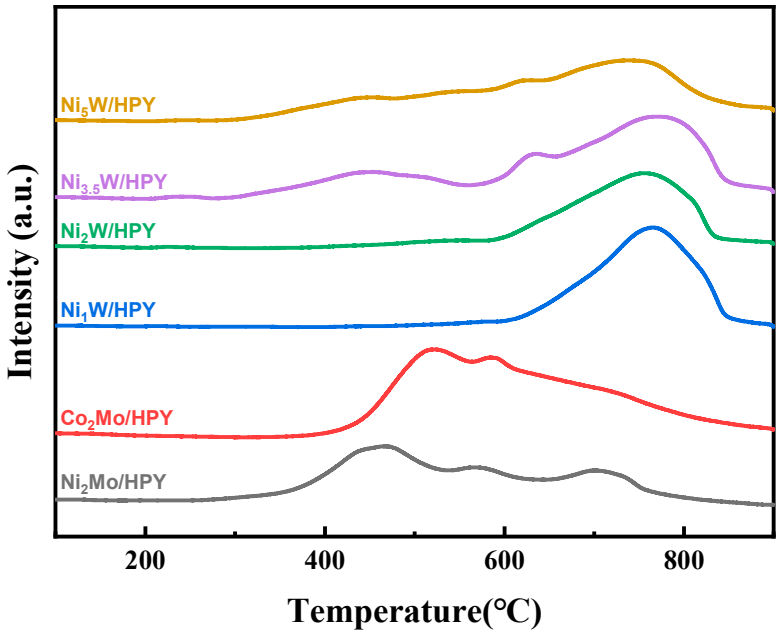



**Figure 4.** $H_2$-TPR characterization of $A_xB/HPY$ series catalysts.

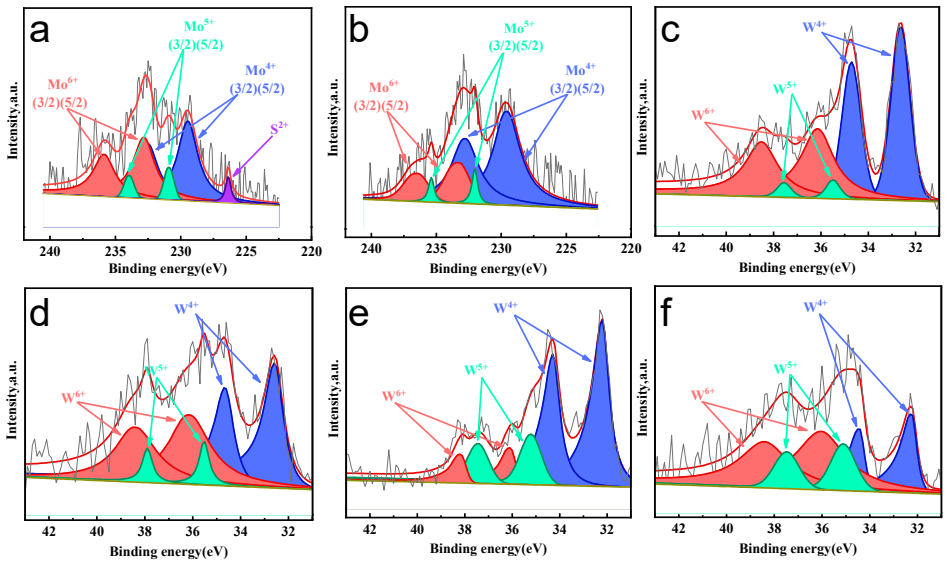



**Figure 5.** Mo(W) XPS spectra of sulfided $A_xB/HPY$ series catalysts: (**a**) $Ni_2Mo/HPY$, (**b**) $Co_2Mo/HPY$, (**c**) $Ni_1W/HPY$, (**d**) $Ni_2W/HPY$, (**e**) $Ni_{3.5}W/HPY$. (**f**) $Ni_5W/HPY$.

**Table 3.** Mo(W) XPS peak data of molybdenum (tungsten) species in sulfided $A_xB$/HPY series catalysts.

| Samples /HPY | Mo(W)$^{4+}$% | Mo(W)$^{5+}$% | Mo(W)$^{6+}$% |
|---|---|---|---|
| $Ni_2Mo$ | 48.8 | 7.1 | 44.1 |
| $Co_2Mo$ | 72.4 | 5.4 | 22.2 |
| $Ni_1W$ | 70.3 | 9.7 | 20.1 |
| $Ni_2W$ | 50.2 | 8.5 | 41.3 |
| $Ni_{3.5}W$ | 52.1 | 5.4 | 42.5 |
| $Ni_5W$ | 59.5 | 26.7 | 13.8 |

### *2.2. Catalytic Performance in Naphthalene Hydrocracking*

Catalytic evaluation in naphthalene hydrocracking demonstrated clear performance differences (Figure 6). $Ni_1W$/HPY delivered exceptional performance, achieving 100% naphthalene conversion across the entire temperature range tested (350–425 °C). Its BTX yield increased with temperature, reaching a maximum of 92.5% at 425 °C. In comparison, $Ni_2Mo$/HPY showed lower naphthalene conversion at the lower temperatures and achieved a maximum BTX yield of 91% at 425 °C. $Co_2Mo$/HPY attained high naphthalene conversion but yielded significantly less BTX than $Ni_2Mo$/HPY. The other $Ni_xW$/HPY catalysts ($Ni_2W$ to $Ni_5W$) maintained high naphthalene conversion (>95% across temperatures) but yielded less BTX than the optimal $Ni_1W$/HPY. Performance deteriorated significantly for $Ni_5W$/HPY. For all catalysts except $Ni_1W$/HPY (already at 100%), naphthalene conversion generally increased with temperature. BTX yield typically peaked at an intermediate temperature (e.g., 425 °C for $Ni_1W$/HPY and $Ni_2Mo$/HPY), beyond which overcracking likely reduced yield.

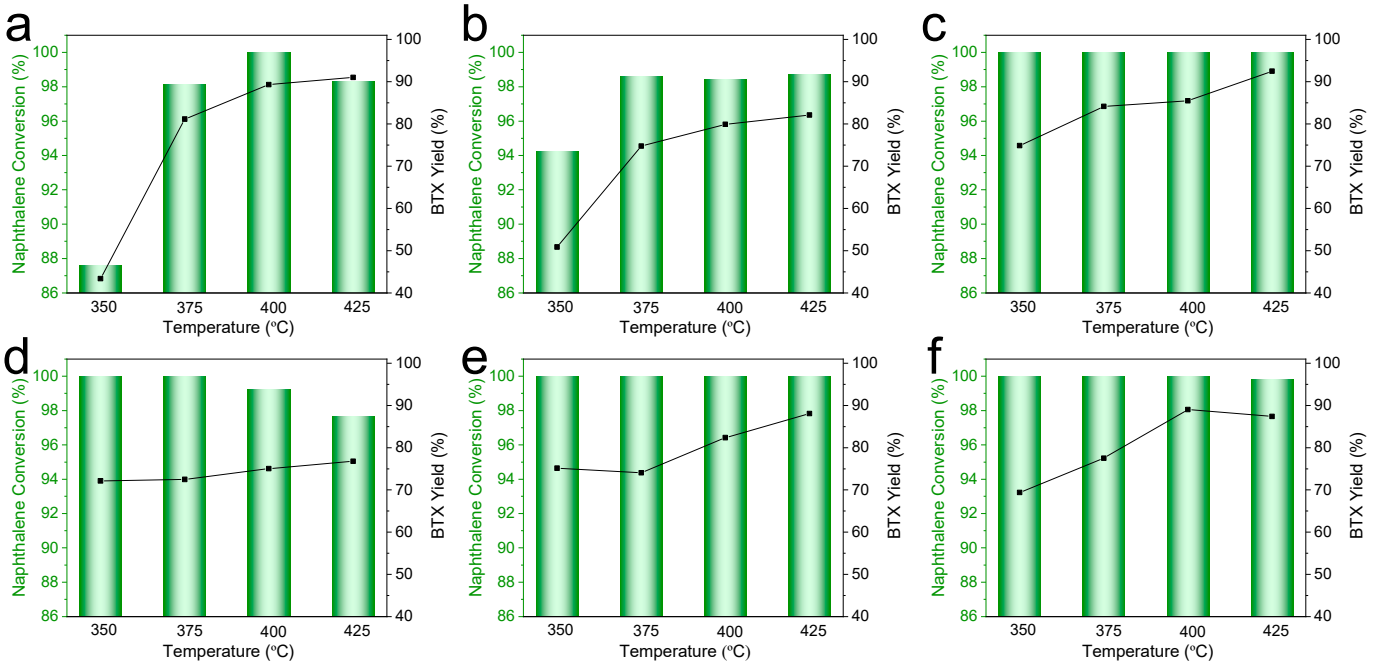



**Figure 6.** Conversion and BTX yield of naphthalene hydrocracking at different reaction temperatures over (**a**) $Ni_2Mo$/HPY, (**b**) $Co_2Mo$/HPY, (**c**) $Ni_1W$/HPY, (**d**) $Ni_2W$/HPY, (**e**) $Ni_{3.5}W$/HPY, and (**f**) $Ni_5W$/HPY.

The outstanding performance of $Ni_1W$/HPY arises from a unique synergy between metal properties and the HPY support, enabling optimal metal–acid balance and spatial separation. The formation of large $WO_3$ crystallites, evident from XRD, and their

preferential location within mesopores and on the external surface of the HPY particle, confirmed by the exceptionally high micropore surface area and volume ($S_{mi}^{c}$ = 427 $m^2/g$, $V_{mi}^{c}$ = 0.20 $cm^3/g$) in $N_2$ physisorption, physically separates the primary hydrogenation sites (sulfided W species in meso/external zones) from the primary cracking sites (strong Brønsted acid sites within the preserved micropores, Py-FTIR: ~196.5 μmol/g strong B-acid). This spatial separation enforces an efficient "hydrogenate then crack" pathway: naphthalene is rapidly hydrogenated to tetralin on the accessible W sites; tetralin diffuses into the micropores where strong Brønsted acids catalyze selective ring-opening and dealkylation to BTX. This separation minimizes undesired deep hydrogenation of tetralin to decalin on metal sites and prevents rapid poisoning of the vital acid sites by metal species or large polyaromatic intermediates. The low Ni loading (1 wt%) is critical: it minimizes Ni agglomeration ($H_2$-TPR: absence of NiO peak) and strong metal–support interaction ($H_2$-TPR: high $WO_3$ reduction temperature), allowing for a high degree of W sulfidation (XPS: 70.25% $W^{4+}$), thereby maximizing the concentration of the active hydrogenation phase ($WS_2$). While higher Ni loadings (x > 1) in $Ni_xW$/HPY improve W dispersion (reduced $WO_3$ XRD peak intensity), they simultaneously strengthen the W-support interaction ($H_2$-TPR peak shift to lower temperature), hinder complete sulfidation (reduced $W^{4+}$ XPS content), and eventually lead to Ni agglomeration ($H_2$-TPR NiO peak), collectively reducing hydrogenation activity and overall catalyst efficiency. Although $Co_2Mo$/HPY demonstrated superior Mo sulfidation (XPS: 72.4% $Mo^{4+}$ vs. $Ni_2Mo$/HPY: 48.8%), likely due to the formation of the highly active "CoMoS" phase, its lower total and strong Brønsted acidity ($NH_3$-TPD, Py-FTIR) compared to $Ni_2Mo$/HPY resulted in inferior cracking performance and consequently lower BTX yield, indicating $Ni_2Mo$/HPY offered a better balance under the specific conditions of this study.

## 3. Experimental Section

### *3.1. Materials*

Naphthalene, cobalt nitrate hexahydrate, ammonium molybdate tetrahydrate, ammonium metatungstate hydrate and nickel nitrate hexahydrate were purchased from Sinopharm Chemical Reagent Co., Ltd. (Beijing, China). USY zeolite was purchased from Shanghai Macklin Biochemical Co., Ltd. (Shanghai, China). hydrochloric acid was purchased from Beijing Chemical Plant (Beijing, China).

### *3.2. HPY Support Synthesis*

USY zeolite was treated with 0.2 mol/L HCl solution at a solid-to-liquid volume ratio of 1:10. The mixture was stirred in a round-bottom flask at 80 °C for 4 h. The solid was then filtered, washed repeatedly with ultrapure water until neutral pH, dried, and calcined to obtain the HPY support.

### *3.3. Catalyst Synthesis (Sequential Incipient Wetness Impregnation)*

In this study, the synthesized catalysts are denoted as AxB/HPY, where 'A' represents the promoter metal (Ni or Co), 'x' denotes the mass fraction (wt%) of the promoter metal oxide (e.g., NiO or CoO), 'B' represents the primary active metal (Mo or W), and HPY stands for the hierarchical porous USY support.

Active metals were loaded onto the HPY support. Total metal oxide loading was fixed at 18.5 wt%. $Ni_2Mo$/HPY (2 wt% NiO/16.5 wt% $MoO_3$), & $Co_2Mo$/HPY(2 wt% CoO/16.5 wt% $MoO_3$): Ammonium heptamolybdate tetrahydrate ($(NH_4)_6Mo_7O_{24}\cdot 4H_2O$) was first dissolved in deionized water, ultrasonically dispersed for 15 min, impregnated onto HPY, followed by ultrasonication, drying, and calcination. After cooling, nickel nitrate hexahydrate ($Ni(NO_3)_2\cdot 6H_2O$) or cobalt nitrate hexahydrate ($Co(NO_3)_2\cdot 6H_2O$) was

dissolved, impregnated, ultrasonicated, dried, and calcined to obtain $Ni_1Mo/HPY$ or $Co_2Mo/HPY$.

$Ni_xW/HPY$ (where x denotes the mass fraction of NiO) Series (x = 1, 2, 3.5, 5): Ammonium metatungstate hydrate ($(NH_4)_6H_2W_{12}O_{40}$) was first dissolved in deionized water, ultrasonically dispersed for 15 min, impregnated onto HPY, followed by ultrasonication, drying, and calcination. After cooling, nickel nitrate hexahydrate ($Ni(NO_3)_2{\cdot}6H_2O$) was dissolved, impregnated, ultrasonicated, dried, and calcined to obtain $Ni_xW/HPY$.

### *3.4. Catalyst Characterization*

The structure and physicochemical properties of the supports and catalysts were investigated using various characterization techniques. These included X-ray diffraction (XRD), transmission electron microscopy (TEM), ammonia temperature-programmed desorption ($NH_3$-TPD), $N_2$ adsorption–desorption isotherms, $H_2$ temperature-programmed reduction ($H_2$-TPR), and X-ray photoelectron spectroscopy (XPS).

The material phase composition of the AxB/HPY series catalysts was characterized by XRD using a Bruker D8 Advance diffractometer (Bruker AXS GmbH, Karlsruhe, Germany) operated at 40 kV and 40 mA, with a scanning rate of 2°/min over a 2θ range of 5–90°. Morphological features were examined by TEM on a Tecnai G2 F20 instrument (Thermo Fisher Scientific, Waltham, MA, USA); samples were ultrasonically dispersed in ethanol and deposited onto carbon-coated copper grids prior to imaging.

Textural properties, including specific surface area and pore size distribution, were determined by $N_2$ physisorption at –196 °C using a Micromeritics TriStar II 2020 analyzer (Micromeritics Instrument Corporation, Norcross, GA, USA). Prior to measurement, samples were degassed at 350 °C under vacuum for 6 h. Surface area was calculated using the BET method, and pore size distribution was derived from the adsorption branch via the Barrett–Joyner–Halenda (BJH) model.

Acidic properties were evaluated by $NH_3$-TPD and Py-FTIR. $NH_3$-TPD was performed using a Tianjin Xianqua TP-5076 system (Tianjin Xianquan Instrument Co., Ltd., Tianjin, China); samples were pretreated at 600 °C under $N_2$, saturated with $NH_3$ at 100 °C, and then heated to 600 °C at 10 °C/min. Py-FTIR spectra were recorded on a Digilab spectrometer (Digilab LLC, Cambridge, MA, USA) after pyridine adsorption and subsequent desorption at 200 °C and 350 °C. Acid site densities were quantified based on integrated peak areas and molar extinction coefficients.

The chemical states of metal species in sulfided catalysts were analyzed by XPS. Binding energies were calibrated against the C 1s peak at 284.8 eV. Reducibility of oxide precursors was assessed by $H_2$ temperature-programmed reduction ($H_2$-TPR), with samples heated to 900 °C under a $H_2$/Ar flow.

### *3.5. Catalytic Evaluation*

Naphthalene hydrocracking was evaluated in a fixed-bed continuous-flow reactor. Catalyst particles (0.5 g, 40–60 mesh) were diluted with quartz sand (2.8 g). Reactions were conducted at 4.0 MPa total pressure, a weight hourly space velocity (WHSV) of 4 $h^{-1}$ (based on naphthalene), and an $H_2$/oil ratio of 600 ($v/v$). The feedstock was 5.0 wt% naphthalene dissolved in n-octane. Reaction temperatures ranged from 350 °C to 425 °C. Liquid products were collected after 4 h on stream for each temperature and analyzed using an Thermal TSQ 8000 EVO gas chromatography mass spectrometry (Thermo Fisher Scientific, Waltham, MA, USA) equipped with an HP-innowax capillary column (30 m × 0.32 mm × 0.25 μm). Carbon balances exceeded 95%. Naphthalene conversion (Conv.%) and product selectivities (Sel.%) were calculated as follows:

$$\text{Conv.\%} = (1 - [\text{Moles of Naphthalene in Product}]/[\text{Moles of Naphthalene in Feed}]) \times 100\%$$

$$\text{Sel.\%} = (\text{Moles of Product i}/\text{Moles of All Detected Products}) \times 100\%$$

$$\text{BTX Yield.\%} = \text{Conv.\%} \times (\text{Sel.Benzene} + \text{Sel.Toluene} + \text{Sel.Xylene})/100$$

## 4. Conclusions

Optimizing the spatial architecture of metal and acid sites within a hierarchical pore-structured catalyst is essential for selective naphthalene hydrocracking to BTX. The superior performance of $Ni_1W$/HPY originates from a unique synergy: large $WO_3$ crystallites located preferentially in mesopores and on external surfaces preserve microporosity, enabling efficient separation of hydrogenation and cracking functions. This structure enforces an optimal 'hydrogenate-then-crack' pathway, minimizing over-cracking and coke formation. While higher Ni loading improves W dispersion, it also induces Ni agglomeration and reduces sulfidation degree, lowering hydrogenation activity. Comparatively, $Co_2Mo$/HPY exhibits higher Mo sulfidation but weaker acidity, resulting in inferior cracking performance. This study highlights the critical balance required between metal dispersion, sulfidation state, acid strength, and pore architecture in designing high-performance bifunctional catalysts for aromatic upgrading.

**Author Contributions:** Conceptualization, H.L. and X.W.; Methodology, K.Z., H.L., X.C. and X.W.; Validation, M.L.; Investigation, K.Z. and M.L.; Writing—original draft, K.Z.; Writing—review & editing, H.L. and X.W.; Visualization, X.W.; Supervision, H.L., X.C. and X.W.; Funding acquisition, H.L. and X.W. All authors have read and agreed to the published version of the manuscript.

**Funding:** This work was supported by the National Natural Science Foundation of China (NSFC, 22409079), the Natural Science Foundation of Shandong Province (ZR2025QC401) and the State Key Laboratory of Heavy Oil Processing (WX20230148 and SKLHOP202401002).

**Institutional Review Board Statement:** Not applicable.

**Informed Consent Statement:** Not applicable.

**Data Availability Statement:** The original contributions presented in this study are included in the article. Further inquiries can be directed to the corresponding authors.

**Conflicts of Interest:** The authors declare no conflict of interest.

## References

1. Peng, C.; Liu, B.; Feng, X.; Du, Y.; Fang, X. Engineering dual bed hydrocracking catalyst towards enhanced high-octane gasoline generation from light cycle oil. *Chem. Eng. J.* **2020**, *389*, 123461. [CrossRef]
2. Zhang, M.; Song, Q.; He, Z.; Wang, Q.; Wang, L.; Zhang, X.; Li, G. Tuning the mesopore-acid-metal balance in Pd/HY for efficient deep hydrogenation saturation of naphthalene. *Int. J. Hydrogen Energy* **2022**, *47*, 20881–20893. [CrossRef]
3. Gordeeva, N.A.; Shesterkina, A.A.; Vikanova, K.V.; Kustov, A.L. Naphthalene and its derivatives hydrogenation for hydrogen storage: Comparative analysis of the role of noble and non-noble metal catalysts—A review. *Int. J. Hydrogen Energy* **2024**, *69*, 113–121. [CrossRef]
4. Gutiérrez, A.; Arandes, J.M.; Castaño, P.; Olazar, M.; Bilbao, J. Preliminary studies on fuel production through LCO hydrocracking on noble-metal supported catalysts. *Fuel* **2012**, *94*, 504–515. [CrossRef]
5. Chen, F.; Huo, J.; Zhao, L.; Gao, J.; Xu, C. Optimizing support acidity of NiMo catalysts for increasing the yield of benzene, toluene and xylene in tetralin hydrocracking. *Front. Chem. Sci. Eng.* **2024**, *18*, 7. [CrossRef]
6. Yu, F.; Zhang, C.; Geng, R.; Zhou, H.; Dong, Q.; Liu, S.; Fan, B.; Li, R. Hydrocracking of naphthalene over Beta zeolite coupled with NiMo/$\gamma$-$Al_2O_3$: Investigation of metal and acid balance based on the composition of industrial hydrocracking catalyst. *Fuel* **2023**, *344*, 128049. [CrossRef]
7. Lee, J.; Choi, Y.; Shin, J.; Lee, J.K. Selective hydrocracking of tetralin for light aromatic hydrocarbons. *Catal. Today* **2016**, *265*, 144–153. [CrossRef]
8. Upare, D.P.; Park, S.; Kim, M.; Jeon, Y.-P.; Kim, J.; Lee, D.; Lee, J.; Chang, H.; Choi, S.; Choi, W. Selective hydrocracking of pyrolysis fuel oil into benzene, toluene and xylene over CoMo/beta zeolite catalyst. *J. Ind. Eng. Chem.* **2017**, *46*, 356–363. [CrossRef]

9. Zhu, L.; Shan, S.; Petkov, V.; Hu, W.; Kroner, A.; Zheng, J.; Yu, C.; Zhang, N.; Li, Y.; Luque, R. Ruthenium–nickel–nickel hydroxide nanoparticles for room temperature catalytic hydrogenation. *J. Mater. Chem. A* **2017**, *5*, 7869–7875. [CrossRef]
10. Shin, J.; Oh, Y.; Choi, Y.; Lee, J.; Lee, J.K. Design of selective hydrocracking catalysts for BTX production from diesel-boiling-range polycyclic aromatic hydrocarbons. *Appl. Catal. A Gen.* **2017**, *547*, 12–21. [CrossRef]
11. Anilkumar, M.; Loke, N.; Patil, V.; Panday, R. Hydrocracking of hydrotreated light cycle oil to mono aromatics over non-noble bi-functional (ni-w supported) zeolite catalysts. *Catal. Today* **2020**, *358*, 221–227. [CrossRef]
12. Oh, Y.; Noh, H.; Park, H.; Han, H.; Nguyen, T.-B.; Lee, J.K. Molecular-size selective hydroconversion of FCC light cycle oil into petrochemical light aromatic hydrocarbons. *Catal. Today* **2020**, *352*, 329–336. [CrossRef]
13. Jia, H.; Yan, W.; Dong, Q.; Qing, B.; Hao, W.; Du, Y.; Zhang, X.; Ma, J.; Li, R. Selective ring-opening in 9, 10-dihydrophenanthrene hydrocracking over a practical NiMo/$Al_2O_3$-USY catalyst under mild conditions. *J. Energy Inst.* **2024**, *116*, 101716. [CrossRef]
14. Kuchinskaya, T.; Kniazeva, M.; Samoilov, V.; Maximov, A. In situ generated nanosized sulfide Ni-W catalysts based on zeolite for the hydrocracking of the pyrolysis fuel oil into the BTX fraction. *Catalysts* **2020**, *10*, 1152. [CrossRef]
15. Golubev, I.; Dik, P.; Kazakov, M.; Pereyma, V.Y.; Klimov, O.; Smirnova, M.Y.; Prosvirin, I.; Gerasimov, E.Y.; Kondrashev, D.; Golovachev, V. The effect of Si/Al ratio of zeolite Y in NiW catalyst for second stage hydrocracking. *Catal. Today* **2021**, *378*, 65–74. [CrossRef]
16. Cao, Z.; Zhang, X.; Xu, C.; Huang, X.; Wu, Z.; Peng, C.; Duan, A. Selective hydrocracking of light cycle oil into high-octane gasoline over bi-functional catalysts. *J. Energy Chem.* **2021**, *52*, 41–50. [CrossRef]
17. Laredo, G.C.; Águeda-Rangel, R.; García-López, A.; García-Gutiérrez, J.L.; Olmos-Cerda, E.H. Effect of the chemical composition of six hydrotreated light cycle oils for benzene, toluene, ethylbenzene, and xylene production by a hydrocracking process. *Appl. Petrochem. Res.* **2021**, *11*, 249–263. [CrossRef]
18. Shanshan, D.; Yongkang, L.; Xun, W.; Ruipeng, R. Effects of W loading amounts on catalytic performances of Ni-W bimetallic catalysts for CH 4-CO 2 reforming reaction. *Low-Carbon Chem. Chem. Eng.* **2024**, *49*, 12–18.
19. Kong, X.; Li, Y.; Liu, Z.; Zou, Y.; Li, D.; Liu, J.; Wang, W.; Wang, C.; Xu, C.; Wang, X. Pore-Structure Engineering of Hierarchical Ni/Y Catalysts for the Enhanced Selective Hydrocracking of Naphthalene to BTX. *ACS Sustain. Chem. Eng.* **2025**, *13*, 23. [CrossRef]
20. Hu, Z.; Hu, P.; Wang, X.; Wu, T.; Ge, S.; Xie, H.; Liu, B.; Chen, S.; Wu, Z. Selective hydrocracking of 1-methylnaphthalene to benzene/toluene/xylenes (BTX) over NiW/Beta bifunctional catalyst: Effects of metal–acid balance. *Fuel* **2024**, *363*, 130947. [CrossRef]
21. Jurković, D.L.; Kostyniuk, A.; Likozar, B. Mechanisms, reaction micro-kinetics and modelling of hydrocracking of aromatic biomass tar model compounds into benzene, toluene and xylenes (BTX) over H-ZSM-5 catalyst. *Chem. Eng. J.* **2022**, *445*, 136898. [CrossRef]
22. Kong, X.; Mei, J.; Liu, Z.; Zou, Y.; Wang, E.; Wang, W.; Wang, C.; Xu, C.; Wang, X. Regulating metal–acid active sites in hierarchical porous Ni/Y for selective hydrocracking of naphthalene. *Carbon Resour. Convers.* **2025**, *8*, 100326. [CrossRef]
23. Chen, F.; Zhang, G.; Weng, X.; Zhang, Y.; Zhao, L.; Cao, L.; Gao, J.; Xu, C.; Liu, X.; Gao, X. High value utilization of inferior diesel for BTX production: Mechanisms, catalysts, conditions and challenges. *Appl. Catal. A Gen.* **2021**, *616*, 118095. [CrossRef]
24. Lee, S.-U.; Lee, Y.-J.; Kim, J.-R.; Jeong, S.-Y. Rational synthesis of silylated Beta zeolites and selective ring opening of 1-methylnaphthalene over the NiW-supported catalysts. *Appl. Catal. B Environ.* **2017**, *219*, 1–9. [CrossRef]
25. Wu, T.; Chen, S.-L.; Yuan, G.-m.; Pan, X.; Du, J.; Zhang, Y.; Zhang, N. High metal–acid balance and selective hydrogenation activity catalysts for hydrocracking of 1-methylnaphthalene to benzene, toluene, and xylene. *Ind. Eng. Chem. Res.* **2020**, *59*, 5546–5556. [CrossRef]
26. Zhang, Y.-T.; Zhang, N.-N.; Chen, S.-L.; Dang, H.; Wu, T. Surface dealuminated Beta zeolites supported WO3 catalyst and its catalytic performance in tetralin hydrocracking. *Pet. Sci.* **2022**, *19*, 3116–3123. [CrossRef]
27. Zhang, Y.; Zhou, Y.; Huang, L.; Zhou, S.; Sheng, X.; Wang, Q.; Zhang, C. Structure and catalytic properties of the Zn-modified ZSM-5 supported platinum catalyst for propane dehydrogenation. *Chem. Eng. J.* **2015**, *270*, 352–361. [CrossRef]
28. Jin, F.; Zhang, P.; Wu, G. Fundamental kinetics model of acidity-activity relation for ethylene oligomerization and aromatization over ZSM-5 zeolites. *Chem. Eng. Sci.* **2021**, *229*, 116144. [CrossRef]
29. Peng, C.; Zhou, Z.; Cheng, Z.; Fang, X. Upgrading of light cycle oil to high-octane gasoline through selective hydrocracking over non-noble metal bifunctional catalysts. *Energy Fuels* **2019**, *33*, 1090–1097. [CrossRef]
30. Klimova, T.; Reyes, J.; Gutiérrez, O.; Lizama, L. Novel bifunctional NiMo/Al-SBA-15 catalysts for deep hydrodesulfurization: Effect of support Si/Al ratio. *Appl. Catal. A Gen.* **2008**, *335*, 159–171. [CrossRef]
31. Ding, L.; Zheng, Y.; Zhang, Z.; Ring, Z.; Chen, J. Hydrotreating of light cycled oil using WNi/Al2O3 catalysts containing zeolite beta and/or chemically treated zeolite Y. *J. Catal.* **2006**, *241*, 435–445. [CrossRef]
32. Arribas, M.a.A.; Concepción, P.; Martínez, A.N. The role of metal sites during the coupled hydrogenation and ring opening of tetralin on bifunctional Pt (Ir)/USY catalysts. *Appl. Catal. A Gen.* **2004**, *267*, 111–119. [CrossRef]

33. Kubička, D.; Kumar, N.; Venäläinen, T.; Karhu, H.; Kubičková, I.; Österholm, H.; Murzin, D.Y. Metal− support interactions in zeolite-supported noble metals: Influence of metal crystallites on the support acidity. *J. Phys. Chem. B* **2006**, *110*, 4937–4946. [CrossRef]
34. Lee, S.-U.; Lee, Y.-J.; Kim, J.-R.; Kim, E.-S.; Kim, T.-W.; Kim, H.J.; Kim, C.-U.; Jeong, S.-Y. Selective ring opening of phenanthrene over NiW-supported mesoporous HY zeolite catalyst depending on their mesoporosity. *Mater. Res. Bull.* **2017**, *96*, 149–154. [CrossRef]
35. Zhengkai, C.; Xia, Z.; Chunming, X.; Aijun, D.; Rong, G.; Zhen, Z.; Ziming, W.; Chong, P.; Jianmei, L.; Xilong, W. The Synthesis of Al-SBA-16 Materials with a Novel Method and Their Catalytic Application on Hydrogenation for FCC Diesel. *Energy Fuels* **2017**, *31*, 805–814.
36. Pedroarena, I.; Grande, L.; Torrez-Herera, J.J.; Korili, S.A.; Gil, A. Analysis by temperature-programmed reduction of the catalytic system Ni-Mo-Pd/$Al_2O_3$. *Fuel* **2023**, *334*, 126789. [CrossRef]
37. Zheng, L.; Li, Z.; Fu, P.; Sun, F.; Liu, M.; Guo, T.; Fan, Q. Development of Mo-modified pseudoboehmite supported Ni catalysts for efficient hydrogen production from formic acid. *ACS Omega* **2022**, *7*, 27172–27184. [CrossRef]
38. Nguyen, H.M.; Pham, G.H.; Ran, R.; Vagnoni, R.; Pareek, V.; Liu, S. Dry reforming of methane over Co–Mo/Al 2 O 3 catalyst under low microwave power irradiation. *Catal. Sci. Technol.* **2018**, *8*, 5315–5324. [CrossRef]
39. Soghrati, E.; Kok Poh, C.; Du, Y.; Gao, F.; Kawi, S.; Borgna, A. C− O Hydrogenolysis of Tetrahydrofurfuryl Alcohol to 1, 5-Pentanediol Over Bi-functional Nickel-Tungsten Catalysts. *ChemCatChem* **2018**, *10*, 4652–4664. [CrossRef]
40. Fang, M.; Ma, S.; Wang, T.; Xia, Z.; Tang, W.; Xia, L.; Luo, Z. Hydrotreatment of model compounds with catalysts of NiW/$Al_2O_3$ and NiWP/$Al_2O_3$ to simulate low temperature coal tar oil. *RSC Adv.* **2017**, *7*, 54512–54521. [CrossRef]
41. De León, J.D.; Picquart, M.; Massin, L.; Vrinat, M.; De los Reyes, J. Hydrodesulfurization of sulfur refractory compounds: Effect of gallium as an additive in NiWS/$\gamma$-$Al_2O_3$ catalysts. *J. Mol. Catal. A Chem.* **2012**, *363*, 311–321. [CrossRef]
42. Tayeb, K.B.; Lamonier, C.; Lancelot, C.; Fournier, M.; Bonduelle-Skrzypczak, A.; Bertoncini, F. Active phase genesis of NiW hydrocracking catalysts based on nickel salt heteropolytungstate: Comparison with reference catalyst. *Appl. Catal. B Environ.* **2012**, *126*, 55–63. [CrossRef]
43. Wang, Y.; Lancelot, C.; Lamonier, C.; Yang, M.; Sun, Y.; Morin, J.-C.; Rives, A. Restraining deactivation of hierarchical zeolite supported NiW catalysts in the HDS of thiophene. *RSC Adv.* **2015**, *5*, 74150–74158. [CrossRef]


**Disclaimer/Publisher's Note:** The statements, opinions and data contained in all publications are solely those of the individual author(s) and contributor(s) and not of MDPI and/or the editor(s). MDPI and/or the editor(s) disclaim responsibility for any injury to people or property resulting from any ideas, methods, instructions or products referred to in the content.